
Performance of a Brain PET Camera Based on Anger-Logic Gadolinium Oxyorthosilicate Detectors

Joel S. Karp, PhD¹; Suleman Surti, PhD¹; Margaret E. Daube-Witherspoon, PhD¹; Richard Freifelder, PhD¹; Christopher A. Cardi, BS¹; Lars-Eric Adam, PhD¹; Kilian Bilger, PhD¹; and Gerd Muehllehner, PhD²

¹Department of Radiology, University of Pennsylvania, Philadelphia, Pennsylvania; and ²Philips Medical Systems, Philadelphia, Pennsylvania

A high-sensitivity, high-resolution brain PET scanner ("G-PET") has been developed. This scanner is similar in geometry to a previous brain scanner developed at the University of Pennsylvania, the HEAD Penn-PET, but the detector technology and electronics have been improved to achieve enhanced performance. **Methods:** This scanner has a detector ring diameter of 42.0 cm with a patient aperture of 30.0 cm and an axial field of view of 25.6 cm. It comprises a continuous light-guide that couples 18,560 (320 × 58 array) 4 × 4 × 10 mm³ gadolinium oxyorthosilicate (GSO) crystals to 288 (36 × 8 array) 39-mm photomultiplier tubes in a hexagonal arrangement. The scanner operates only in 3-dimensional (3D) mode because there are no interplane septa. Performance measurements on the G-PET scanner were made following National Electrical Manufacturers Association NU 2-2001 procedures for most measurements, although NU 2-1994 procedures were used when these were considered more appropriate for a brain scanner (e.g., scatter fraction and counting-rate performance measurements). **Results:** The transverse and axial resolutions near the center are 4.0 and 5.0 mm, respectively. At a radial offset of 10 cm, these numbers deteriorate by approximately 0.5 mm. The absolute sensitivity of this scanner measured with a 70-cm long line source is 4.79 counts per second (cps)/kBq. The scatter fraction measured with a line source in a 20-cm-diameter × 19-cm-long cylinder is 39% (for a lower energy threshold of 410 keV). For the same cylinder, the peak noise equivalent counting rate is 60 kcps at an activity concentration of 7.4 kBq/mL (0.20 μCi/mL), whereas the peak true coincidence rate is 132 kcps at an activity concentration of 14 kBq/mL (0.38 μCi/mL). Images from the Hoffman brain phantom as well as ¹⁸F-FDG patient scans illustrate the high quality of images acquired on the G-PET scanner. **Conclusion:** The G-PET scanner attains the goal of high performance for brain imaging through the use of an Anger-logic GSO detector design with continuous optical coupling. This detector design leads to good energy resolution, which is needed in 3D imaging to minimize scatter and random coincidences.

Key Words: PET; brain imaging; gadolinium oxyorthosilicate

J Nucl Med 2003; 44:1340-1349

Received Oct. 8, 2002; revision accepted Mar. 28, 2003.

For correspondence or reprints contact: Joel S. Karp, PhD, Department of Radiology, Hospital of the University of Pennsylvania, 3400 Spruce St., Philadelphia, PA 19104.

E-mail: karp@rad.upenn.edu

A dedicated brain scanner can provide images with high spatial resolution, while also providing a counting-rate capability sufficient to study physiologic effects with fast temporal dynamics. Dedicated brain PET scanners with a small detector ring diameter provide large solid-angle coverage of the human head, leading to higher sensitivity per unit detector volume when compared with a multipurpose whole-body PET scanner (1). The increased sensitivity achieved by such scanners comes with decreased noncollinearity degradation of the spatial resolution but with greater parallax and solid-angle effects. The reduced cost and complexity of a small ring design make dedicated brain scanners desirable for use in many imaging procedures, both clinical and research. However, there is a potential drawback of such a small ring design—namely, increased scatter and random coincidence fractions. To minimize the increase in scatter and random coincidences, particularly in 3-dimensional (3D) imaging, it is necessary to use a scintillation detector with good energy and timing resolutions, in addition to high stopping power. Gadolinium oxyorthosilicate (GSO) is such a scintillator.

In an effort to achieve high isotropic spatial resolution and sensitivity in a cost-effective design, our group previously developed a dedicated brain scanner, the HEAD Penn-PET (2,3), using a continuous NaI(Tl) detector. The HEAD Penn-PET scanner was fully 3D (no septa), was stationary (no wobbling), and used analog (Anger-logic) position encoding. To compensate for the lower stopping power of NaI(Tl), the scanner had a small detector diameter (42 cm) and a large axial field of view (FOV) (25.6 cm) to achieve a large solid angle of acceptance and, thus, a high geometric sensitivity. Also, the higher light output of NaI(Tl) allowed us to use large photomultiplier tubes (PMTs) (50-mm diameter), thus minimizing the cost and complexity of the instrument. Very good spatial resolution in the reconstructed image of <4 mm (isotropic) was achieved with this design. In addition, the good energy resolution allowed the use of a higher energy threshold to minimize scatter and randoms (4). An energy threshold of 450 keV used with the

HEAD Penn-PET limited the scatter fraction to 34% with a standard 20-cm-diameter phantom. The real drawback of the scanner was its counting-rate capability due to pulse pileup in NaI(Tl) (5) at activity levels greater than 37 MBq (1 mCi) in the imaging FOV.

This article describes the performance of a new brain scanner that was designed to overcome the HEAD Penn-PET's major limitation of counting-rate capability by improving the detector technology and electronics. Using a similar system geometry and building on the experience gained with the HEAD Penn-PET scanner, we have developed a new, high-sensitivity, high-resolution brain PET scanner ("G-PET") using a discrete GSO crystal-based Anger-logic detector (6). Preliminary data and further details on the scanner design have been published (7). Our design was guided by the goal to achieve high system sensitivity and high (isotropic) spatial resolution, coupled with high counting-rate capability. Strong consideration was also given to practical issues and reliable operation of the system.

GSO was developed in 1983 (8) and was shown to have favorable properties for PET in terms of stopping power and decay time, as shown in Table 1. Although used in the Scanditronix PC-1024 systems (alongside bismuth germanate [BGO] crystals) (11), the interest in GSO for PET applications dropped off quickly. For 2-dimensional (2D) PET, stopping power is most important, and BGO, with its high linear attenuation coefficient, is ideal in that regard. In 2D PET, scattered radiation is rejected by septa, so good energy resolution is not critical. Also, the counting rate is limited by the low sensitivity due to septa, not by dead-time effects, so a short crystal decay time is not essential. For these reasons, the use of GSO was abandoned in 2D PET scanners. However, for 3D imaging, scanner performance depends on a more complicated relationship among stopping power, energy resolution, and timing characteristics. GSO has a good combination of these 3, although it is not best in any one. GSO has better energy resolution than another commonly used scintillator, lutetium oxyorthosilicate (LSO) (10% full width at half maximum [FWHM] at 511 keV, compared with 12% FWHM for LSO (9)), even

though its light output is relatively low compared with that of LSO. LSO, on the other hand, has better spatial resolution and timing. Perhaps most importantly, the uniformity of light output with GSO is excellent because of improvements by Hitachi Chemical Co. in manufacturing and polishing (12,13), which impacts on the overall system performance. In a measurement of the light output of >20,000 crystals from which we selected those used in the brain scanner, <7% variation (SD) in light output was found. These properties, together with the fact that GSO is not very sensitive to temperature variations, as reported earlier (14), make GSO a very favorable and practical choice for a high-performance, 3D imaging PET scanner.

The following sections describe the design and performance of the G-PET scanner.

MATERIALS AND METHODS

Scanner Design

Detector, Electronics, and Position Processing. Like the HEAD Penn-PET, the G-PET scanner has a detector ring diameter of 42.0 cm and an axial FOV of 25.6 cm. It operates only in 3D mode without interplane septa. A total of 18,560 GSO crystals (58 rings of 320 crystals) and 288 PMTs (8 rows \times 36 columns in a hexagonal lattice) are coupled to a single annular light-guide. The crystals are $4 \times 4 \times 10$ mm³, and the PMTs are 39 mm in diameter. Short crystals were chosen to reduce the parallax error that increases with smaller ring diameters. The light-guide thickness is 1.9 cm with 5-mm-deep slots cut in both the transverse and the axial dimensions. The light-guide thickness and slots were chosen empirically to produce the best crystal discrimination (6). A cross section of the GSO-based Anger-logic detector is shown schematically in Figure 1A. The patient port of the scanner is restricted to 30 cm, and a 2.5-cm-thick lead side shield is used to reject events from activity outside the FOV.

The electronics for the G-PET scanner were built by Philips Medical Systems and are based on the methodologies of signal processing and position calculation used on the Penn-PET scanners developed during the 1980s (15–18). The scanner is electronically split into 6 virtual, overlapping detectors, although the light-guide, crystals, and PMTs form a single, continuous ring. The output from each PMT enters the preamplifiers that lack the pulse-clipping circuits that were needed with NaI(Tl) scintillators but are otherwise identical to those described previously (16). The signals from the PMTs are then passed to the digitizers. An op-amp shaping circuit designed for the GSO pulse shapes the PMT signals. Pulse shaping for the GSO signal is performed to make the pulse more symmetric, so that sampling by the flash (asynchronous) analog-to-digital converters (ADCs) is adequate to produce good energy resolution for the scanner, although this method does not achieve as good energy resolution as using gated integration. Pulse shaping is also used to reduce the tail of the GSO signal that results from a decay time of 65 ns. The shaping circuit lies directly on the digitizer board where the flash ADCs sample the shaped PMT signals. The clock speed for the G-PET electronics has been doubled from the 25 MHz (40-ns sampling interval) used with the NaI(Tl) scanners to 50 MHz (20-ns sampling interval). Concurrently, the analog preamplifier outputs from the PMTs are also summed into 36 overlapping trigger channels, each consisting of a group of 15 PMTs. The overlapping triggering scheme (19), together with the good system energy

TABLE 1

Comparison of Physical Properties of NaI(Tl), LSO, GSO, and BGO Scintillators

Physical property	NaI(Tl)	LSO	GSO	BGO
Attenuation coefficient (cm ⁻¹)	0.35	0.86	0.70	0.95
Energy resolution at 662 keV (%)	6.6*	10	8.5	10.2
Decay time (ns)	230	40	60	300

*Energy resolution for signal after pulse clipping is 9%.

Decay time given for GSO corresponds to cerium concentration of 0.5 mol%. Energy resolution measurements are for single, Teflon (DuPont)-wrapped crystals on PMT. Data are from (9,10). Measurements for NaI(Tl) and GSO are consistent with published results.

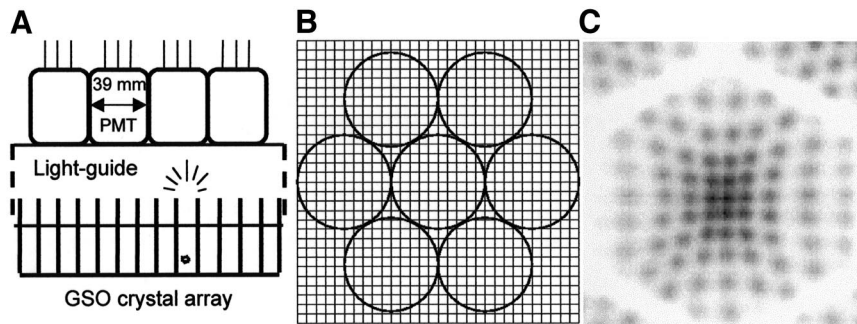


FIGURE 1. GSO Anger-logic detector. (A) Cross-sectional schematic of detector, showing GSO crystal array, annular light-guide, and PMT array. Crystal dimensions are $4 \times 4 \times 10 \text{ mm}^3$, PMTs are 39-mm diameter in hexagonal grid, and light-guide thickness (including slots) is 19 mm. (B) View of one 7-PMT cluster of continuous hexagonal PMT array (other PMTs not shown) overlaying crystal grid. Each PMT sees many crystals, and local 7-PMT cluster is used to determine energy and position of interaction. (C) Flood image with coarse position sampling. Image is linearly distorted with gaps between PMT regions due to use of Anger logic for position determination, but crystals are well discriminated.

resolution, provides the capability to raise the hardware trigger threshold before energy correction to as high as 400 keV, thereby reducing the scanner dead time significantly. Once a coincidence has been detected, the specific trigger channels (in coincidence) define a select group of ADCs, which are summed to obtain the total light emitted (deposited energy) from each of the 2 interactions, followed by calculations of the local energy and local position centroid (16). These are calculated using signals from a cluster of 7 PMTs (Fig. 1B); the central PMT in the cluster is the PMT that receives the maximum amount of light from the event. As described earlier, the light-guide thickness was chosen so that very little light spreads beyond these 7 PMT signals. Note that energy and position are not calculated for every event, but only for those in coincidence. For transmission scanning, however, the scanner is run in a singles mode where these calculations are performed for every event that triggers the electronics.

Data Calibrations. Three types of corrections are performed before the data are binned into a sinogram format. These are PMT gain matching, energy correction, and crystal boundary determination. First, the PMT signals are corrected for gain variations by adjusting the preamplifier outputs to compensate for the PMT signal amplitude. The gains are calibrated by requiring that the calculated local energy (sum of 7 PMT signals) for a point source of activity in the center of the scanner FOV be uniform over the entire detector. A total of 288 small regions on the detector are sampled, each region near the center of a PMT. The calibration is repeated iteratively by adjusting the PMT gains until the local energies for all regions are the same. The PMT gain matching is important to achieve optimum crystal separation as well as good energy resolution. Figure 1C shows a flood image for 1 PMT region (with part of adjacent PMT regions seen in the corners). Very good crystal discrimination is obtained. The gaps that appear between PMTs are due to the nonlinear behavior of the local centroid algorithm in positioning an event near the boundary of a PMT, because in this region the position calculation is sensitive to which PMT cluster is chosen for the event.

Once the position and deposited energy of an interaction have been calculated, a position-dependent energy correction is performed via a lookup table. Energy correction compensates mainly for systematic variations in the light collection from crystals near a PMT center compared with those crystals near the PMT edge, where some light is lost in the open space between PMTs. In

principle, this correction can be used to account for variations in the light output of individual crystals. However, we do not match the size of the energy correction bin to the size of the crystal, because our measurements have shown that the SD of the light output of the crystals used in G-PET is small ($<7\%$) and, during assembly, care was taken to place crystals of similar light outputs next to each other. Figures 2A and 2B show a 2D energy flood before and after energy correction, respectively. The variation in measured energy is $<20\%$ between a PMT center and its edge. Figure 2C shows the local energy spectrum before and after energy correction for a 511-keV source, averaged over the entire detector. The local energy resolution averaged over the detector is $<18\%$ at 511 keV after energy correction. This allows us to set the lower energy threshold in software to 410 keV.

The final data correction involves identification of crystal boundaries. This must take into consideration the spatial nonlinearity of the calculated position, which is a characteristic of all Anger-logic detectors. For this purpose, we developed an automated search algorithm that detects the minima (between crystals) within a high-count flood histogram, defines the crystal boundaries around each crystal, and assigns a real position to all events that occur within each boundary region. The procedure must also properly identify crystals that lie exactly between 2 PMTs and appear in 2 adjacent PMT regions in the flood image.

After all of these corrections have been performed, the acquired data from the scanner are binned into a sinogram with 320 angles, 63 rays, up to 15 out-of-plane tilt angles, and 115 axial slices. The radial samples are 4.4 mm apart in the center of the scanner and closer together toward the edge. The axial pitch of the 58 crystal rows is also 4.4 mm for an axial slice separation of 2.2 mm. Transverse interleaving is performed to improve the radial sampling at the expense of angular sampling; the $320 \text{ angles} \times 63 \text{ rays}$ are resorted into $160 \text{ angles} \times 125 \text{ rays}$. After transverse interleaving, the radial bins are 2.2 mm apart in the center of the scanner (closer together at the edge). To remove the nonuniform radial sampling and to generate a sinogram compatible with pre-existing software, data interpolation is performed before further data corrections (normalization, scatter, and attenuation) and reconstruction. During interpolation, the 125 radial bins (unevenly sampled) are interpolated to 256, 1-mm (evenly sampled) bins; 160 angles are interpolated to 192 angles; and 115 slices are interpolated to 128, 2-mm slices. Because this interpolation step causes a

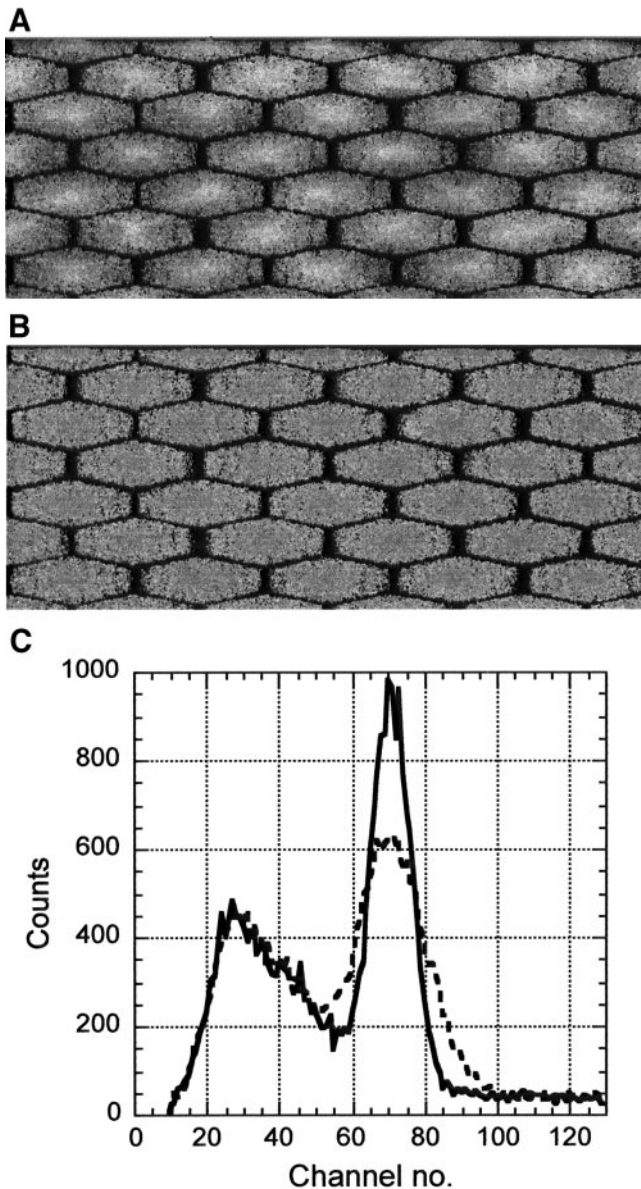


FIGURE 2. (A) 2D energy flood before energy correction. (B) 2D energy flood after energy correction. (C) Measured energy spectrum for scanner of 511-keV source before (dashed line) and after (solid line) energy correction. Average energy resolution after energy correction is 18% over whole detector.

small loss in spatial resolution, this step may be eliminated in the future, as iterative reconstruction algorithms do not require uniform data sampling. The binning into 15 out-of-plane tilts is also an approximation, because each bin covers approximately 3.7° (maximum acceptance angle, $\pm 28^\circ$). Axial binning into tilt angles may be eliminated in the near future, as well, to improve axial resolution.

Corrections for Scatter, Random Coincidences, and Attenuation. For routine clinical scans, correction for randoms and scatter is performed using a background tail-fitting algorithm similar to that developed for the HEAD Penn-PET scanner (3). Although simple in concept, this algorithm is surprisingly robust for clinical brain studies. Research studies, however, demand improved accu-

racy and span a greater range of counting rates where random coincidences often become a more significant factor. The G-PET has the capability of online randoms subtraction, using a delayed coincidence window technique, which, together with a model-based scatter correction (20), affords us the potential for more accurate quantification. These techniques have been developed and are currently being evaluated.

Attenuation correction for clinical studies is often performed using a calculated method, based on the skull outline. However, transmission scans can be performed when quantification is important. For this purpose, we have implemented the singles method (21–23) using a ^{137}Cs transmission point source. The advantages of using ^{137}Cs over a positron emitter are a higher photon flux, an improved ability to acquire postinjection transmission scans due to the different energies of the transmission and emission sources (662-keV transmission vs. 511-keV emission), and the 30-y half-life, which reduces the cost of the device by eliminating the need to replace the source as it decays. The source holder is made of tungsten that provides fanbeam collimation between the 740-MBq (20 mCi) source and patient and shields the back detectors. The source is located near the edge of the axial FOV (close to the shoulders) and, with each rotation, which takes 40 s, we sort and store transmission data over an axial dimension of 64 mm. Therefore, a full scan of the head (including the neck) typically requires 3 scans (1 rotation each), axially offset by 64 mm. Initially, single-slice rebinning (SSRB) (24) and ordered-subsets expectation maximization reconstruction (25) have been implemented, following the example of clinical whole-body studies. However, we have demonstrated in previous studies with the HEAD Penn-PET scanner, which has the same large axial acceptance angle, that Fourier rebinning (FORE) (26) can be applied to transmission data (23) and results in higher accuracy. In fact, the optimal reconstruction technique might be cone beam reconstruction to avoid any axial resolution losses due to rebinning. Investigation of these alternative approaches is being pursued for the G-PET in an effort to improve quantification further.

Several factors must be considered with singles transmission scanning. First, attenuation coefficients must be converted from 662 to 511 keV, which can be done to good approximation by a linear scaling. Also, even with a narrow energy window, some emission contamination (at 511 keV) is measured in the transmission energy window (600–800 keV). To compensate for this, we perform a mock scan. This is a transmission scan acquired with the transmission source retracted, in which the emission contamination (EC) in the transmission energy window is measured and subsequently subtracted. This EC scan requires an additional 24 s per bed position after the transmission scan. We have recently developed an alternative method of estimating the EC, which has little structure, from the singles rates; this does not require a separate EC scan for each patient and reduces the overall transmission scan time. For a typical ^{18}F -FDG study, the EC fraction, relative to transmission, is about 6%–12%. After these corrections, the transmission scan is reconstructed and segmented, using a histogram-based algorithm such as that used with coincidence transmission data (27). Segmentation is inherently capable of compensating for bias in the attenuation values, which helps to minimize the effect of scatter in the fully 3D transmission data. An increased scatter fraction would lead to an underestimation of the measured attenuation values. The key feature of our segmentation algorithm (28) is a histogram fit, which assumes that the soft-tissue peak in the histogram can be automatically determined. In addition to correct

assignment of tissue and skull attenuation values, statistical fluctuations are removed; thus, noise in the transmission scan is not propagated to the emission image. The segmentation algorithm described by Bilger et al. (28) has been tested with the G-PET and found to provide accurate attenuation correction. Figure 3A shows the reconstructed transmission data acquired in 3 bed positions (1 min per position), whereas Figure 3B shows the removal of the statistical fluctuations and a more accurate assignment of attenuation factors in the segmented image. Although the initial focus has been to improve the accuracy of the transmission scan with the segmentation algorithm, there is the potential to shorten the scan time below 40 s per rotation, as well, though this will require modifications to the transmission bearing and motor apparatus.

3D Reconstruction. For routine clinical image reconstruction, we have implemented a fast version of a fully 3D iterative reconstruction algorithm, the row action maximum likelihood algorithm (RAMLA) (29–31). Image representation using smooth basis functions provides an alternative approach that can reduce the computational demands of 3D iterative approaches. This image representation allows utilization of a more advantageous spatial grid, compared with the classical voxel (simple cubic) grid. It also can lead to a more uniform 3D distribution of the basis functions throughout the 3D space by using a body-centered cubic grid based on the effective spatial sampling. This, in turn, allows one to decrease the grid density (number of grid points) without compromising the quality of the image representation. The differences in image quality between the 2 grids are not visually perceptible, yet the difference in reconstruction speed is significant: about a factor of 5, to 10 min for a $256 \times 192 \times 128 \times 15$ sinogram into a $128 \times 128 \times 128$ image using a standard workstation computer (SUN Blade 1000; Sun Microsystems, Inc.). The image reconstruction time is important when one considers that most of the scans with ^{11}C -ligands will be acquired dynamically with multiple time frames.

Scanner Performance Measurements

Performance measurements were performed on the G-PET scanner, following the procedures outlined in the new National Electrical Manufacturers Association (NEMA) NU 2–2001 standard (32,33), where appropriate. However, as noted in the NU 2–2001 standard, which emphasizes whole-body imaging, the scatter fraction and counting-rate measurements for dedicated brain imaging devices with a small transverse FOV should be performed with the NEMA NU 2–1994 procedures (34,35). In a brain scanner, the shorter, cylindric 20-cm-diameter \times 19-cm-long phantom more closely simulates the clinical brain imaging activity distribution,

in contrast to the 70-cm-long phantom prescribed in the NU 2–2001 standard. The energy window was 410–665 keV, except as noted.

Spatial Resolution. Spatial resolution measurements were performed using a point source of ^{18}F in a thin glass capillary tube with an inner diameter of <1 mm. The axial length of the point source was also kept to <1 mm. Following the NEMA NU 2–2001 protocol, measurements were performed with the source in air at radial positions of 1 and 10 cm; data were acquired at a radius of 7 cm as well. The data were acquired in 15 tilt angles, and the sinograms were reconstructed using the 3D Fourier reprojection (3D-FRP) algorithm (36), with an unapodized filter (ramp filter with a cutoff at the Nyquist frequency). We also reconstructed the point source data with FORE followed by filtered backprojection (2D-FBP) for comparison. FORE is commonly used in 3D PET; however, this algorithm is not used on the G-PET scanner because it suffers from losses in axial resolution.

The FWHM and full width at tenth maximum (FWTM) of the point-spread function were determined in all 3 directions by forming 1-dimensional response functions through the peak of the distribution in the 3 orthogonal directions. The profile width at right angles to the direction of measurement was ~ 2 times the FWHM in those directions, as specified by the NEMA NU 2–2001 standard, rather than a single pixel. The FWHM and FWTM were calculated by linear interpolation between adjacent pixels at one half or one tenth of the maximum value of the response function. This maximum value was determined by a parabolic fit using the peak value and its 2 nearest neighboring points.

Scatter. The scatter fraction for the G-PET scanner was measured following the NEMA NU 2–1994 procedure, which specifies a line source filled with ^{18}F , placed at 3 radial positions (0, 45, and 90 mm) within a water-filled, 20-cm-diameter \times 19-cm-long cylindrical phantom. Note that this phantom does not extend the full length of the G-PET scanner, which has a 25.6-cm axial FOV. However, we believe that this phantom best represents the scatter seen by the scanner for brain studies. The data were acquired at low counting rates and rebinned using SSRB. The total number of events, N_{total} , and the number of scattered coincidences, S_c , within a 24-cm diameter (4 cm larger than the phantom diameter) were calculated from the sinogram, as prescribed by the NU 2–1994 standard. The scatter fraction, SF , was then calculated by:

$$SF = \frac{S_c}{N_{total}} \quad \text{Eq. 1}$$

NEMA NU 2–2001 scatter measurements with a 70-cm-long, 3.9-mm-diameter line source in a 20-cm-diameter \times 70-cm-long cylinder of polyethylene were also performed as a function of the lower energy threshold (E_{min}) while keeping the upper energy threshold fixed at 665 keV. The data were acquired at low counting rates and rebinned with SSRB; the processing and analysis were the same as above.

Sensitivity. Following the NEMA NU 2–2001 standard, the absolute sensitivity (counting rate per activity) of the G-PET scanner was measured using a 70-cm-long line source at the center of the scanner, with and without 4 metal sleeves of different thicknesses, representing varying amounts of attenuation. Linear regression was used to fit the natural logarithm of the counts as a function of sleeve thickness to obtain an extrapolated value (for no absorber) for the absolute sensitivity of the scanner.

The scanner sensitivity was also measured using the 20-cm-

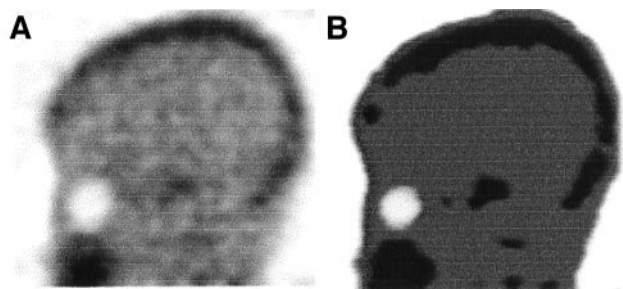


FIGURE 3. Reconstructed transmission image (A) and transmission image after segmentation (B) using histogram algorithm. In these images, areas of high attenuation are dark, and areas of low attenuation are light.

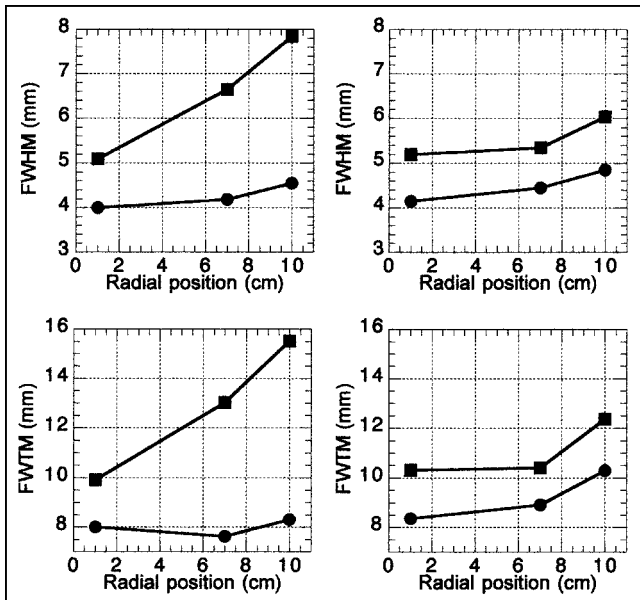


FIGURE 4. Spatial resolution measurements for point source in G-PET scanner (following NEMA NU 2–2001 protocol). Measured FWHM and FWTM are shown in top and bottom, respectively, in reconstructed images. Data were reconstructed by 2D-FBP after FORE (left) and 3D-FRP (right). ●, Transverse resolution; ■, axial resolution.

diameter \times 19-cm-long NEMA cylinder, following the NEMA NU 2–1994 protocol. This cylinder was uniformly filled with water containing a small, known amount of ^{18}F . Data were collected at a low counting rate so that random coincidences were negligible. The scatter fraction previously measured for this phantom was used to correct for the scattered events in the collected sinograms and, thus, estimate the true coincidences, from which the sensitivity per activity concentration in the phantom could be calculated.

Counting-Rate Performance. As noted above, for counting-rate measurements, we used a 20-cm-diameter \times 19-cm-long cylinder uniformly filled with water and ^{18}F . The initial activity was 111 MBq (3 mCi); dynamic scans were acquired over several half-lives of the ^{18}F isotope. The background fraction, determined by tail fitting (37), at low activity levels is equal to the scatter fraction; at higher activities, the background fraction includes contributions from random coincidences. The noise equivalent counting (NEC) rate (38) was then calculated using the formula:

$$NEC = \frac{T \times T}{T + Sc + kR}, \quad \text{Eq. 2}$$

where T , Sc , and R are the true, scatter, and randoms counting rates, respectively; k was taken to be 1, because the background fraction is determined by a smooth fit to the data, so the estimate of random coincidences can be assumed to be noise free.

Hoffman Brain Phantom. The 3D Hoffman brain phantom (39) was filled with about 37 MBq (1 mCi) and scanned for 45 min (\sim 500 million collected events). The data were reconstructed using the 3D RAMLA reconstruction algorithm.

Patient Study. For illustration, we have included a clinical brain scan of a 70-kg patient after the injection of 296 MBq (8 mCi) ^{18}F -FDG. There was no diagnosis of brain disease for this patient. Scanning began after an uptake period of 45 min with an acqui-

sition collection rate (true + scatter + randoms) of about 200 kilocounts per second (kcps), for a collection of 235 million total events after 20 min. To date, we have performed about 400 clinical brain studies on this scanner.

RESULTS

Spatial Resolution

Figure 4 summarizes the results of the spatial resolution measurement. From Figure 4 we see that the spatial resolution of the G-PET scanner, using 3D-FRP, near the center of the FOV is 4.1 mm in the transverse direction and 5.2 mm in the axial direction. At a radius of 10 cm, the transverse resolution degrades to 4.7 mm, and the axial resolution is 5.8 mm. Note that when FORE is performed followed by 2D-FBP, the axial resolution degrades to 7.7 mm at a radius of 10 cm. The uncertainty in the measurements of FWHM and FWTM is ± 0.2 mm. For comparison, the spatial resolution FWHM (with the same data) using a narrow profile, as specified in the NEMA NU 2–1994 procedure, is 3.7 mm in the transverse direction and 5.0 mm in the axial direction.

Scatter

The scatter fraction value in the central slices is 48%, 46%, and 33% for source positions at $r = 0, 45,$ and 90 mm, respectively. The average scatter fraction for the scanner using the weighting scheme described in the NEMA NU 2–1994 standard is 39% (over the central 17 cm of the scanner axial FOV) for an energy window of 410–665 keV.

The scatter fraction results for the 70-cm-long phantom are shown as a function of lower energy threshold in Figure 5A. Also shown is the relative true sensitivity, normalized to the value for a lower energy threshold of 410 keV. Raising the lower energy threshold (E_{\min}) initially leads to a slow decrease in the true sensitivity but a significant decrease in the scatter fraction. For example, the scatter fraction value decreases from about 46% for $E_{\min} = 410$ to 30%

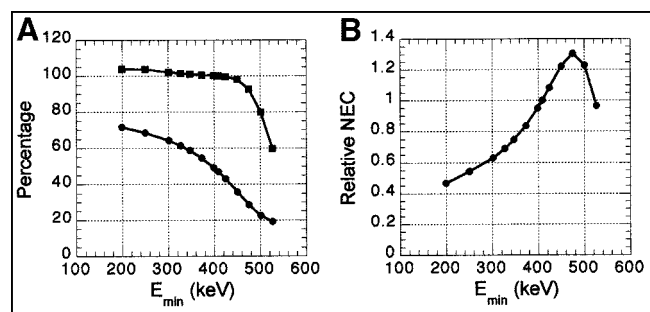


FIGURE 5. Study of impact of lower energy threshold (E_{\min}) on performance. (A) Relative true sensitivity (■) and scatter fraction (●) as function of E_{\min} for 70-cm-long line source in 20-cm-diameter \times 70-cm-long polyethylene cylinder. Relative true sensitivity is sensitivity normalized to sensitivity for $E_{\min} = 410$ keV. (B) Relative NEC as function of E_{\min} calculated for data taken with 70-cm-long line source in 20-cm-diameter \times 70-cm-long polyethylene cylinder. Relative NEC is normalized to NEC for $E_{\min} = 410$ keV.

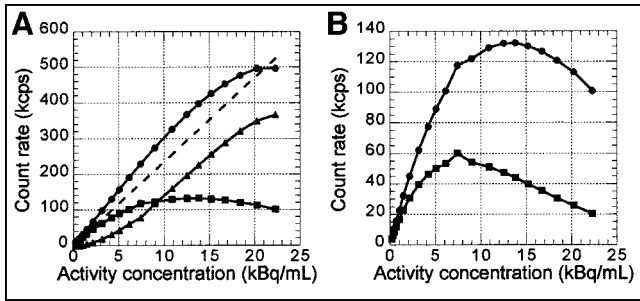


FIGURE 6. Counting-rate curves for G-PET scanner as measured with uniform 20-cm-diameter \times 19-cm-long cylindrical phantom, following NEMA NU 2-1994 protocol. (A) Total (●), true (■), and random (▲) coincidence rates are plotted as function of activity concentration in phantom. Also shown is true rate, extrapolated to case of no dead-time losses (dashed line). (B) True (●) and NEC (■) rates as function of activity concentration.

for $E_{\min} = 475$ keV, with a decrease of $<10\%$ in the sensitivity. The 70-cm cylinder measurement was also used to calculate the NEC value at this low activity concentration as a function of E_{\min} . Figure 5B shows the relative NEC (normalized to the value at $E_{\min} = 410$ keV) calculated as a function of E_{\min} . These results show that by raising E_{\min} to 475 keV there is a potential 25% gain in the NEC value over an E_{\min} of about 410 keV. These results suggest that the relative loss in true sensitivity with a very high E_{\min} will be more than offset by the reduction of scattered events, for an overall improvement of image quality. It should be noted that the calculation of NEC for Figure 5B did not include random coincidences because the measurement was taken at low counting rates. A higher E_{\min} will also reduce random coincidences, for an even greater improvement in NEC than that shown.

Sensitivity

The absolute sensitivity of the G-PET scanner is 4.79 cps/kBq. The axial sensitivity profile is a triangular function

and peaks in the center of the FOV at 0.08 cps/kBq (3 kcps/mCi). However, this sensitivity measurement is normalized to the total activity present in the 70-cm-long line source. Because the scanner axial FOV is 25.6 cm, the absolute sensitivity for activity within the FOV will be about 3 times higher than the value obtained with a 70-cm-long source.

Following the NEMA NU 2-1994 procedure with the 20-cm-diameter \times 19-cm-long cylinder, the sensitivity per activity concentration is 20 kcps/kBq/mL (680 kcps/ μ Ci/mL). Because the length of this phantom is shorter than the axial FOV of the G-PET scanner, the measured sensitivity is lower than what would be obtained if the phantom filled the entire FOV. The maximum slice sensitivity (2.0-mm slices) for this phantom in G-PET is about 0.4 kcps/kBq/mL (16 kcps/ μ Ci/mL) near the center of the FOV.

Counting-Rate Performance

Figure 6 summarizes the results of the counting-rate measurement. The true rate peaks at 132 kcps at an activity concentration of 13.69 kBq/mL (0.37 μ Ci/mL), and the NEC rate peaks at 60 kcps at an activity concentration of 7.40 kBq/mL (0.20 μ Ci/mL).

Hoffman Brain Phantom

Figure 7 shows representative slices of the 3D Hoffman brain phantom acquired on the G-PET scanner. The very accurate delineation of substructures in these images illustrates the high spatial resolution and image quality attained by this scanner.

Patient Study

Figure 8 shows selected transverse, sagittal, and coronal slices from the patient study with ^{18}F -FDG. High image contrast and spatial resolution lead to good visual quality in routine clinical scans. A 20-min scan provides very high image quality and excellent delineation of small structures.

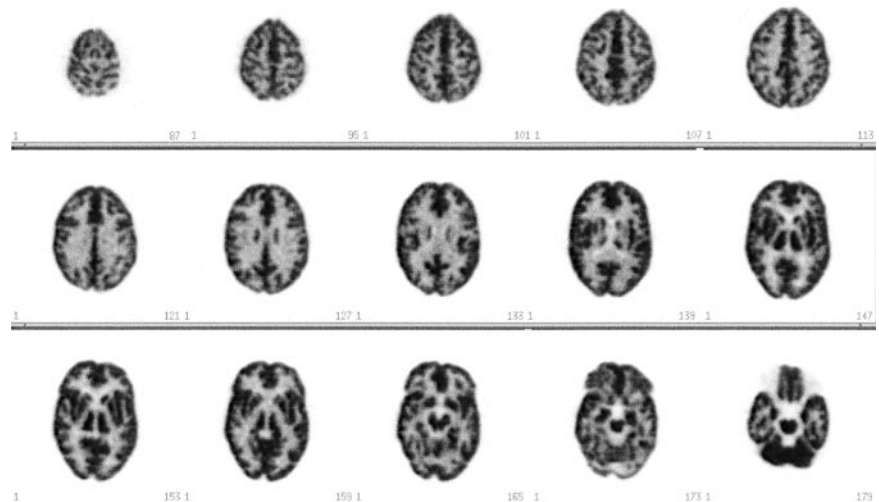


FIGURE 7. Selected transverse slices from reconstructed image of Hoffman brain phantom measured with G-PET scanner. Images were reconstructed with 3D RAMLA.

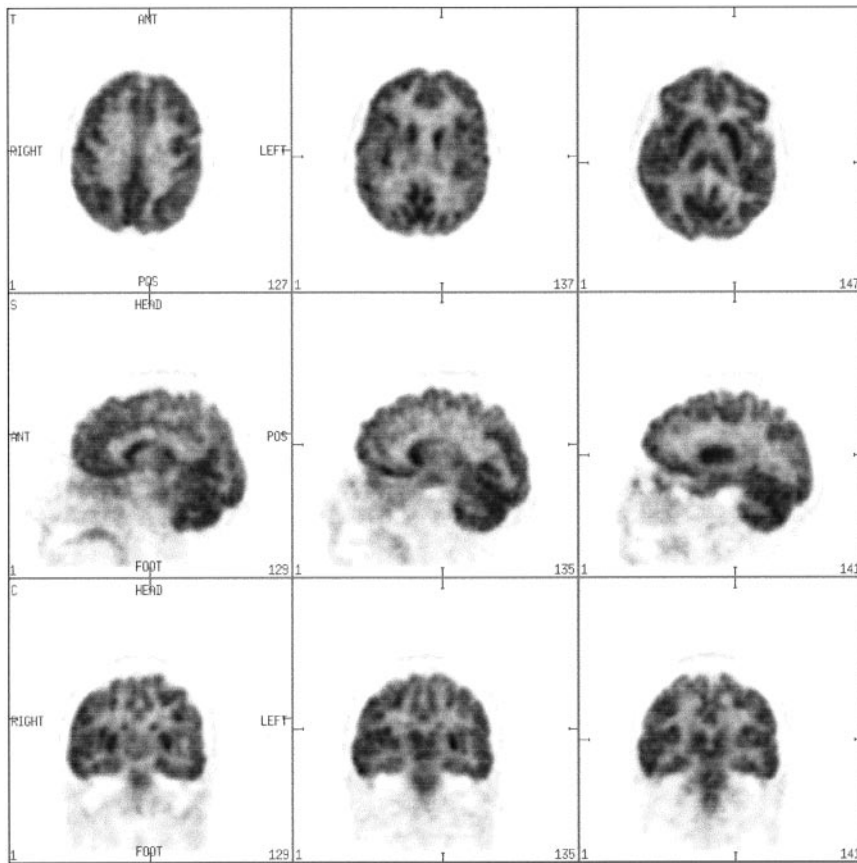
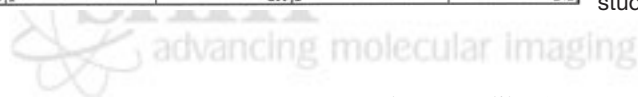


FIGURE 8. Selected transverse (top row), sagittal (middle row), and coronal (bottom row) slices from ^{18}F -FDG patient study, diagnosed without brain disease.



DISCUSSION

The G-PET scanner represents a departure from the use of large area detectors of NaI(Tl) to small, discrete crystals in a ring geometry. The detector design is unlike a block detector, however, in that a light-guide is used between the arrays of crystals and PMTs to control the spread of the light. This permits the use of a smaller number of (larger) PMTs with more crystals seen by each PMT and eliminates the edge effects seen at the edges of the blocks.

The NEMA resolution measurement specifies that the image pixel size should be smaller than one third of the expected FWHM. We reconstructed the images into a $256 \times 256 \times 128$ array where the pixel size is 1 mm in the transverse direction and 2 mm in the axial direction. Thus, the NEMA requirement was satisfied in the transverse direction, but not in the axial direction, which we expect to have a small degrading effect on the measurement of axial resolution.

Like the transverse resolution, the axial resolution worsens slightly at a radial distance of 10 cm due to depth-of-interaction effects. The results from the 3D-FRP reconstruction show more uniform axial resolution across the transverse FOV than those obtained with 2D-FBP after FORE. Note that FORE distorts the shape of the point-spread function; the axial resolution worsens, whereas the transverse resolution degrades only slightly as the radial distance increases. For clinical studies, 3D RAMLA is used

because, like 3D-FRP, it preserves uniform spatial resolution within the FOV, but it provides images with lower noise than 3D-FRP. Resolution results for 3D RAMLA were not included because the measured spatial resolution for an iterative reconstruction algorithm can depend strongly on the local activity distribution when the algorithm is not run to convergence (40). Even with fully 3D data acquisition and reconstruction, there is some loss of intrinsic spatial resolution due to rebinning approximations and practical data storage considerations. However, these limitations may be eliminated in the near future, as the iterative algorithms are modified to handle nonuniform sampling of the data.

Our study of the effect of E_{\min} on scatter fraction and NEC indicates the possibility of a reduction in scatter and gain in NEC by raising E_{\min} up to 475 keV. However, implementation of the higher E_{\min} will require an evaluation of the stability of the energy peak in the scanner. The daily quality control for the scanner issues a warning for a peak drift of more than $\pm 2\%$. We are currently investigating how much peak drift can be tolerated when the energy threshold is raised. In addition, further improvements to the energy resolution, which are also under study, would permit an increased E_{\min} and lead to lower scatter and better NEC.

We have achieved our goal of surpassing the performance of the HEAD Penn-PET scanner, which was based on an

annular, continuous NaI(Tl) detector. Compared with the HEAD Penn-PET scanner, the G-PET scanner has similar spatial resolution, somewhat higher sensitivity, even with short crystals, but significantly higher counting-rate capability. The light response function is tuned through the design of the light-guide to restrict the light spread to the local cluster of PMTs. The choice of 39-mm PMTs represents a trade-off between the goal to increase counting-rate capability (which requires small PMTs) and the need to maintain the cost and complexity of the system (which argues for large PMTs). This is due to the faster decay of GSO and the very narrow light response function of the pixelated detector design, both of which reduce pulse pileup and detector dead time. As a comparison, for a 20-cm-diameter \times 19-cm-long phantom, the maximum true counting rate increases by about a factor of 4, compared with that for the HEAD Penn-PET, to approximately 132 kcps, whereas the scatter and randoms fractions remain similar. It is notable that with the HEAD Penn-PET scanner dead-time considerations limit the injected activity of ^{18}F -FDG to only 110 MBq (3 mCi) for a 70-kg patient, whereas with the G-PET scanner we have increased the dose to 370 MBq (10 mCi). For shorter-lived isotopes, including ^{11}C -ligands and ^{15}O -water, we can inject higher doses but will be limited by randoms, rather than dead time, as can be seen in Figure 6. It needs to be emphasized that, although GSO is significantly more expensive than NaI(Tl), the performance enhancements of the G-PET scanner, compared with the HEAD Penn-PET, are achieved while containing the cost of the scanner through the use of relatively few PMTs and associated electronic channels.

CONCLUSION

A high-performance brain scanner using the GSO Anger-logic detector has been developed. The small detector diameter and large axial FOV leads to a large solid angle, with a maximum out-of-plane angular acceptance of $\pm 28^\circ$. The performance measurements show that this scanner has excellent spatial resolution, coupled with high sensitivity, which combine to lead to good image quality. The combination of high spatial resolution and high sensitivity are essential to achieve both good image quality and accurate quantification. In addition, brain perfusion studies with ^{15}O -water, as well as studies using other short-lived isotopes such as ^{11}C , will require this scanner to operate at high counting rates to achieve a good signal-to-noise ratio for imaging rapidly changing processes. With the fast signal decay time of GSO, together with the restricted light spread in the detector design, the G-PET scanner is capable of reaching high coincidence data rates.

ACKNOWLEDGMENTS

We thank the following individuals from Philips Medical Systems, Philadelphia, who helped support this project by helping to test and debug hardware and software that was

specially modified for the G-PET: Ben Chase, Michael Geagan, Tom Heal, Steve Martin, Matthew Werner, Mike Parma, and Kay Rainford. We also thank Dr. Paul Vaska (Philips Medical Systems, Philadelphia) and Fang Liu (University of Pennsylvania) for their help in crystal testing, Chris DiGrazio (Philips Medical Systems, Philadelphia) for help with scanner construction, and Dr. Samuel Matej (University of Pennsylvania) for guidance in the application of the 3D RAMLA and 3D-FRP reconstruction algorithms. This work was supported by the Counter Drug Technology Assessment Center, an office within the Office of National Drug Control Policy, and by U.S. Department of Energy grant DE-FG02-88ER60642.

REFERENCES

- Hoffman EJ, Phelps ME, Huang SC. Performance evaluation of a positron tomograph designed for brain imaging. *J Nucl Med.* 1983;24:245–257.
- Freifelder R, Karp JS, Geagan M, Muehllehner G. Design and performance of the head PENN-PET scanner. *IEEE Trans Nucl Sci.* 1994;41:1436–1440.
- Karp JS, Freifelder R, Geagan MJ, et al. Three-dimensional imaging characteristics of the HEAD PENN-PET scanner. *J Nucl Med.* 1997;38:636–643.
- Karp JS, Kinahan PE, Muehllehner G, Countryman P. Effect of increased axial-field of view on the performance of a volume PET scanner. *IEEE Trans Med Imaging.* 1993;12:299–306.
- Mankoff DA, Muehllehner G, Karp JS. The high count rate performance of a two-dimensionally position-sensitive detector for positron emission tomography. *Phys Med Biol.* 1989;34:437–456.
- Surti S, Karp JS, Freifelder R, Liu F. Optimizing the performance of a PET detector using discrete GSO crystals on a continuous lightguide. *IEEE Trans Nucl Sci.* 2000;47:1030–1036.
- Surti S, Karp JS, Adam L-E, Muehllehner G. Performance measurements for the GSO-based brain PET camera (G-PET). In: Siebert JA, ed. *2001 IEEE Nuclear Science Symposium and Medical Imaging Conference Record.* Piscataway, NJ: The Institute of Electrical and Electronics Engineers, Inc.; 2002:M2-6.
- Takagi K, Fukazawa T. Cerium-activated Gd_2SiO_5 single crystal scintillator. *App Phys Lett.* 1983;42:43–45.
- Moszynski M, Kapusta M, Wolski D, Szawlowski M, Klamra W. Energy resolution of scintillation detectors readout with large area avalanche photodiodes and photomultipliers. *IEEE Trans Nucl Sci.* 1998;45:472–477.
- van Eijk CWE. Inorganic scintillators in medical imaging. *Phys Med Biol.* 2002;47:R85–R106.
- Holte S, Ostertag H, Kesselberg M. A preliminary evaluation of a dual crystal positron camera. *J Comput Assist Tomogr.* 1987;11:691–697.
- Ishibashi H, Shimizu K, Susa K, Kubota S. Cerium doped GSO scintillators and its application to position sensitive detectors. *IEEE Trans Nucl Sci.* 1989;36:170–172.
- Kurashige K, Kurata Y, Ishibashi H, Susa K. Mechanical properties of a Gd_2SiO_5 single crystal. *Jpn J Appl Phys.* 1997;36:2242–2246.
- Melcher CL, Schweitzer JS, Manente RA, Peterson CA. Applicability of GSO scintillators for well logging. *IEEE Trans Nucl Sci.* 1991;38:506–509.
- Muehllehner G, Colsher JG. Use of position-sensitive detectors in positron imaging. *IEEE Trans Nucl Sci.* 1980;NS-27:569–571.
- Karp JS, Muehllehner G, Beerohm D, Mankoff D. Event localization in a continuous scintillation detector using digital processing. *IEEE Trans Nucl Sci.* 1986;33:550–555.
- Mankoff DA, Muehllehner G, Karp JS. The effect of detector performance on high count rate PET imaging with a tomograph based on position-sensitive detectors. *IEEE Trans Nucl Sci.* 1988;35:592–597.
- Mankoff DA, Muehllehner G, Miles GE. A local coincidence triggering system for PET tomographs composed of large-area position-sensitive detectors. *IEEE Trans Nucl Sci.* 1990;37:730–736.
- Surti S. *A Model of Scintillation Detector Performance for Positron Emission Tomography* [PhD thesis]. Philadelphia, PA: Department of Physics, University of Pennsylvania; 2000.
- Accorsi R, Adam L-E, Karp JS. Implementation of a single scatter simulation algorithm for 3D PET: application to emission and transmission. In: Metzler S, ed. *2002 IEEE Nuclear Science Symposium and Medical Imaging Conference Record.* Piscataway, NJ: The Institute of Electrical and Electronics Engineers, Inc.; 2003:M3-186.

21. Karp JS, Muehllehner G, Qu H, Yan X-H. Singles transmission in volume imaging PET with a Cs-137 source. *Phys Med Biol.* 1995;40:929–944.
22. Smith RJ, Karp JS. Post-injection transmission scans in a PET camera operating without septa with simultaneous measurement of emission activity contamination. *IEEE Trans Nucl Sci.* 1996;43:2207–2212.
23. Karp JS, Becher AJ, Matej S, Kinahan PE. Data processing and image reconstruction methods for the HEAD PENN-PET scanner. *IEEE Trans Nucl Sci.* 1998;45:1144–1151.
24. Daube-Witherspoon ME, Muehllehner G. Treatment of axial data in three-dimensional PET. *J Nucl Med.* 1987;28:1717–1724.
25. Hudson HM, Larkin RS. Accelerated image reconstruction using ordered subsets of projection data. *IEEE Trans Med Imaging.* 1994;13:601–609.
26. Defrise M, Kinahan PE, Townsend DW, Michel C, Sibomana M, Newport DF. Exact and approximate rebinning algorithms for 3D PET data. *IEEE Trans Med Imaging.* 1997;11:145–158.
27. Bilger K, Kupferschlag J, Muller-Schauenburg W, Nusslin F, Bares R. Threshold calculation for segmented attenuation correction in PET with histogram fitting. *IEEE Trans Nucl Sci.* 2001;48:43–50.
28. Bilger K, Adam L-E, Karp JS. Segmented attenuation correction using Cs-137 single photon transmission. In: Siebert JA, ed. *2001 IEEE Nuclear Science Symposium and Medical Imaging Conference.* Piscataway, NJ: The Institute of Electrical and Electronics Engineers, Inc.; 2002:M13B-19.
29. DePierro AR. On some nonlinear iterative relaxation methods in remote sensing. *Matematica Aplicada e Computacional.* 1989;8:153–166.
30. Browne JA, DePierro AR. A row-action alternative to the EM algorithm for maximizing likelihoods in emission tomography. *IEEE Trans Med Imaging.* 1996;15:687–699.
31. Daube-Witherspoon ME, Matej S., Karp JS. Assessment of image quality with a fast fully 3D reconstruction algorithm. In: Siebert JA, ed. *2001 IEEE Nuclear Science Symposium and Medical Imaging Conference.* Piscataway, NJ: Institute of Electrical and Electronics Engineers, Inc.; 2002:M14-2.
32. National Electrical Manufacturers Association. *NEMA Standards Publication NU 2–2001: Performance Measurements of Positron Emission Tomographs.* Rosslyn, VA: National Electrical Manufacturers Association; 2001.
33. Daube-Witherspoon ME, Karp JS, Casey ME, et al. PET performance measurements using the NEMA NU 2–2001 standard. *J Nucl Med.* 2002;43:1398–1409.
34. National Electrical Manufacturers Association. *NEMA Standards Publication NU 2–1994: Performance Measurements of Positron Emission Tomographs.* Washington, DC: National Electrical Manufacturers Association; 1994.
35. Karp JS, Daube-Witherspoon ME, Hoffman EJ, et al. Performance standards in positron emission tomography. *J Nucl Med.* 1991;32:2342–2350.
36. Matej S, Lewitt RM. Direct Fourier reconstruction with Fourier reprojection for fully 3-D PET. *IEEE Trans Nucl Sci.* 2001;48:1378–1385.
37. Karp JS, Muehllehner G, Mankoff DA, et al. Continuous-slice PENN-PET: a positron tomograph with volume imaging capability. *J Nucl Med.* 1990;31:617–627.
38. Strother SC, Casey ME, Hoffman EJ. Measuring PET scanner sensitivity: relating count rates to image signal-to-noise ratios using noise equivalent counts. *IEEE Trans Nucl Sci.* 1990;37:783–788.
39. Hoffman EJ, Cutler PD, Digby WM, Mazziotta JC. 3-D phantom to simulate cerebral blood flow and metabolic images for PET. *IEEE Trans Nucl Sci.* 1990;37:616–620.
40. Liow JS, Strother SC. The convergence of object-dependent resolution in maximum likelihood based tomographic reconstruction. *Phys Med Biol.* 1993;38: 55–70.

